Available online at www.sciencedirect.com
ScienceDirect
Cement & Concrete Composites 30 (2008) 465–477
Cement & Concrete Composites
www.elsevier.com/locate/cemconcomp

# Correlation of tensile and flexural responses of strain softening and strain hardening cement composites

Chote Soranakom, Barzin Mobasher *

*Department of Civil and Environmental Engineering, Arizona State University, Tempe, AZ 85287, United States*

Received 3 May 2007; received in revised form 22 January 2008; accepted 23 January 2008
Available online 6 February 2008

**Abstract**

Closed form equations for generating moment–curvature response of a rectangular beam of fiber reinforced concrete are presented. These equations can be used in conjunction with crack localization rules to predict flexural response of a beam under four point bending test. Parametric studies simulated the behavior of two classes of fiber reinforced concrete: strain softening and strain hardening materials. The simulation revealed that the direct use of uniaxial tension and compression responses under-predicted the flexural response for strain softening material while a good prediction for strain hardening material was obtained. The importance of strain softening range on the flexural response is discussed using non-dimensional post-peak parameters. Results imply that the brittleness and size effect are more pronounced in the flexural response of brittle materials, while more accurate predictions are obtained with ductile materials. It is also demonstrated that correlations of tensile and flexural results can be established using normalized uniaxial tension and compression models with a single scaling factor.


*Keywords:* Fiber reinforced concrete; Uniaxial tension test; Bending test; Flexural behavior; Moment–curvature response

## 1. Introduction

Reinforcement of cementitious materials with short randomly distributed fibers has been successfully practiced for more than 40 years [1,2]. Due to the low fracture toughness of cement-based materials, tensile cracks occur easily due to applied stress, restraint, or environmental conditions. The interfacial bond developed between the fibers and matrix utilizes the strength and stiffness of the fibers in reinforcing the brittle matrix. Once the matrix cracks, load still transfers across the crack faces through the bridging fibers. As the load on the composite is increased, the process of fiber pullout affects load carrying capacity and further contributes to energy dissipation. It has also been known when using a high volume fraction of fibers with a high specific surface area, the crack bridging potential and the strength of the composite are increased [3–5]. An increase in volume fraction of the fiber shows an enhancement of tensile strength in a variety of discrete fiber systems, including Steel Fiber Reinforced Concrete (SFRC) [6–8], Glass Fiber Reinforced Concrete (GFRC) [9], Slurry Infiltrated Mat Concrete (SIMCON) [10,11], Ductal [12] and Engineered Cementitious Composite (ECC) [13–15]. Similar behaviors are also observed in continuous fiber systems such as Ferrocement (FRC) [16] and Textile Reinforced Cements (TRCs) [17,18], which show improved tension capacity and ductility. In the continuous systems, the increase in strength is associated with distributed cracking mechanisms and strain hardening behavior [19].

The non-linear behavior of fiber reinforced concrete is best characterized by closed loop controlled tests conducted in tension or flexure. Fig. 1a presents tensile stress–strain response as compared to equivalently elastic flexural stress vs. deflection of Alkali Resistant (AR) glass fabric reinforced composite material [20]. It is critically important to observe that the general shapes of these

* Corresponding author. Tel.: +1 480 965 0141; fax: +1 480 965 0557.
*E-mail addresses:* chote@asu.edu (C. Soranakom), barzin@asu.edu (B. Mobasher).

0958-9465/$ - see front matter © 2008 Elsevier Ltd. All rights reserved.
doi:10.1016/j.cemconcomp.2008.01.007

**Nomenclature**

| | |
|---|---|
| $b$ | beam width |
| $C$ | a parameter for normalized moment in Table 6 |
| $c$ | a parameter to define localized crack zone |
| $D$ | a parameter for neutral axis depth ratio in Table 6 |
| $d$ | beam depth |
| $E$ | tensile modulus |
| $E_c$ | compressive modulus |
| $E_{ci}$ | initial compressive modulus |
| $E_{cr}$ | post-crack tensile modulus |
| $F$ | force component |
| $f$ | stress at vertex in stress diagram |
| $h$ | height of each zone in stress diagram |
| $I$ | moment of inertia |
| $k$ | neutral axis depth ratio |
| $L$ | clear span |
| $M_{cr}$ | moment at first cracking |
| $M_{fail}$ | moment at failure |
| $M'_i$ | normalized moment $M/M_{cr}$ |
| $M_{low}$ | moment at the lowest point before continue the 2nd ascending curve |
| $M_{max}$ | maximum moment in moment–curvature diagram |
| $M_{max1}, M_{max2}$ | local maximum moment 1 and 2 in moment–curvature diagram |
| $P$ | total load applied to four point bending beam specimen |
| $S$ | spacing in four point bending test |
| $y$ | moment arm from neutral axis to center of each force component |
| $\alpha$ | normalized transition strain |
| $\beta$ | normalized tensile strain at bottom fiber |
| $\beta_{tu}$ | normalized ultimate tensile strain |
| $\varepsilon_c$ | compressive strain |
| $\varepsilon_{cr}$ | first cracking tensile strain |
| $\varepsilon_{ctop}$ | compressive strain at the top fiber |
| $\varepsilon_{cu}$ | ultimate compressive strain |
| $\varepsilon_{cy}$ | compressive yield strain |
| $\varepsilon_t$ | tensile strain |
| $\varepsilon_{tbot}$ | tensile strain at bottom fiber |
| $\varepsilon_{trn}$ | strain at transition point |
| $\varepsilon_{tu}$ | ultimate tensile strain |
| $\gamma$ | normalized compressive strain |
| $\eta$ | normalized post-crack modulus |
| $\lambda$ | normalized compressive strain |
| $\lambda_{cu}$ | normalized ultimate compressive strain |
| $\sigma_c$ | compressive stress |
| $\sigma_{cr}$ | cracking tensile strength |
| $\sigma_{cst}$ | constant tensile stress at the end of tension model |
| $\sigma_{cy}$ | compressive yield stress |
| $\sigma_t$ | tensile stress |
| $\omega$ | normalized compressive yield strain |
| $\xi$ | unloading factor |

*Subscripts*

t1, t2, t3 tension zone 1, 2, 3

c1, c2 compression zone 1, 2

1, 21, 22, 31, 32 stage 1, 2.1, 2.2, 3.1, 3.2 according to the value of $\beta$

curves are similar as they represent initial linear portions followed by a range with a reduced stiffness that is due to distributed cracking. There is however a fundamental difference in the magnitudes of stress from the tests and the associated deformations. The two main parameters characterizing the tensile response are the first cracking tensile strength or Bend Over Point (BOP) and the Ultimate Tensile Strength (UTS). In the flexural loading case, the first cracking is referred to as the Limit of Proportionality (LOP) and ultimate strength as the Modulus of Rupture (MOR). The fact that the MOR value may be several times higher than the ultimate tensile strength UTS can be attributed to several parameters, including the nature of data reduction, size effect, and also nature of the loading. This discrepancy has been well known in the field [21]. This phenomenon is best shown by comparing the cumulative probability distribution functions for the four strength parameters. The distribution of BOP and UTS in tension followed by LOP and MOR in flexure are shown in Fig. 1b using the results from thin section fabric cement composites [20]. Note that there are fundamental over-predictions of first cracking and ultimate strength in flexure as compared to the tension case by as much as 300%. These indicate that use of flexural data as fundamental material properties in the design of cement composites may be misleading and unconservative. Closed form relationships that explain such differences between the tensile and flexural strengths have been recently proposed by the authors for both strain hardening [22,23] and strain softening type composites [24]. The present formulation combines and extends the available modeling techniques using a unified approach.

In order to correlate tensile and flexural data for various materials, a unified closed form solution for generating moment–curvature response of homogenized materials is presented for various fiber reinforced composite systems. Since the solution is derived explicitly, iterative procedures required for handling material non-linearity are not necessary; hence this method is attractive for use in an inverse analysis algorithm to back-calculate material parameters from convenient flexural tests. Furthermore, the moment–curvature response generated by closed form solution can be used as an input section property for a beam element in non-linear finite element analysis to predict flexural

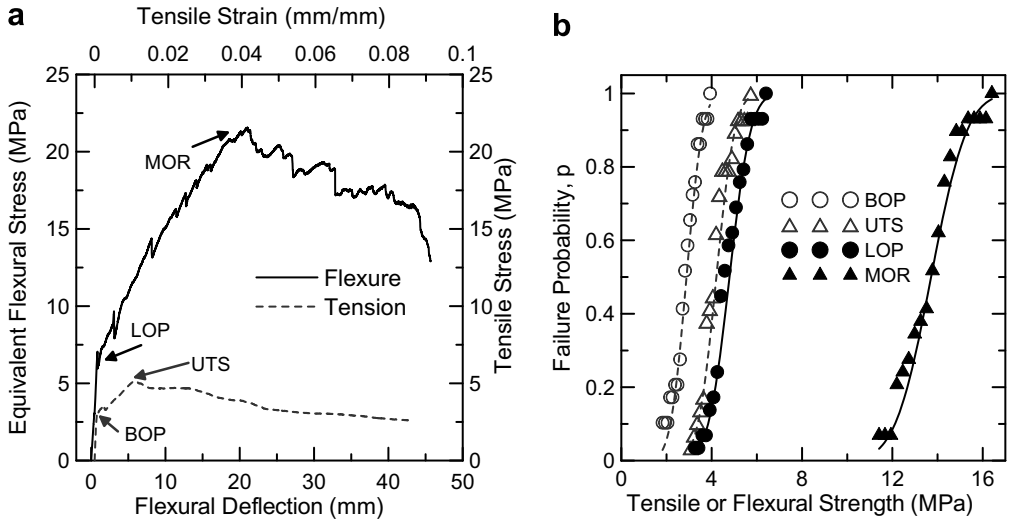


Fig. 1. Relationship between uniaxial tension test and flexural test of fabric reinforced cement: (a) comparison of experimental responses and (b) comparison of cumulative probability distributions for LOP, MOR, BOP, and UTS [20].

behavior of more complex structures. Finally, the closed form solutions of the proposed equations can be subsequently used in a simplified design procedure for cement composites.

## 2. Derivation of closed form solutions for moment–curvature diagram

Fig. 2 presents a constitutive model for homogenized strain softening and hardening fiber reinforced concrete. As shown in Fig. 2a, the linear portion of an elastic–perfectly plastic compressive stress–strain response terminates at yield point ($\varepsilon_{cy}$, $\sigma_{cy}$) and remains constant at compressive yield stress $\sigma_{cy}$ until the ultimate compressive strain $\varepsilon_{cu}$. The tension model in Fig. 2b is described by a trilinear response with an elastic range defined by $E$, and then post-cracking modulus $E_{cr}$. By setting $E_{cr}$ to either a negative or a positive value, the same model can be used to simulate strain softening or strain hardening materials. The third region in the tensile response is a constant stress range defined with stress $\sigma_{cst}$ in the post-crack region. The constant stress level $\mu$ can be set to any value at the transition strain, resulting in a continuous or discontinuous stress response. Two strain measures are used to define the first cracking and transition strains ($\varepsilon_{cr}, \varepsilon_{trn}$). The tensile response terminates at the ultimate tensile strain level of $\varepsilon_{tu}$. The stress–strain relationship for compression and tension can be expressed as

$$\sigma_c(\varepsilon_c) = \begin{cases} E_c\varepsilon_c & 0 \leqslant \varepsilon_c \leqslant \varepsilon_{cy} \\ E_c\varepsilon_{cy} & \varepsilon_{cy} < \varepsilon_c \leqslant \varepsilon_{cu} \\ 0 & \varepsilon_c > \varepsilon_{cu} \end{cases} \tag{1}$$

$$\sigma_t(\varepsilon_t) = \begin{cases} E\varepsilon_t & 0 \leqslant \varepsilon_t \leqslant \varepsilon_{cr} \\ E\varepsilon_{cr} + E_{cr}(\varepsilon_t - \varepsilon_{cr}) & \varepsilon_{cr} < \varepsilon_t \leqslant \varepsilon_{trn} \\ \mu E\varepsilon_{cr} & \varepsilon_{trn} < \varepsilon_t \leqslant \varepsilon_{tu} \\ 0 & \varepsilon_t > \varepsilon_{tu} \end{cases} \tag{2}$$

where $\sigma_c$, $\sigma_t$, $\varepsilon_c$ and $\varepsilon_t$, are compressive and tensile stresses and strains, respectively. In order to derive the closed form

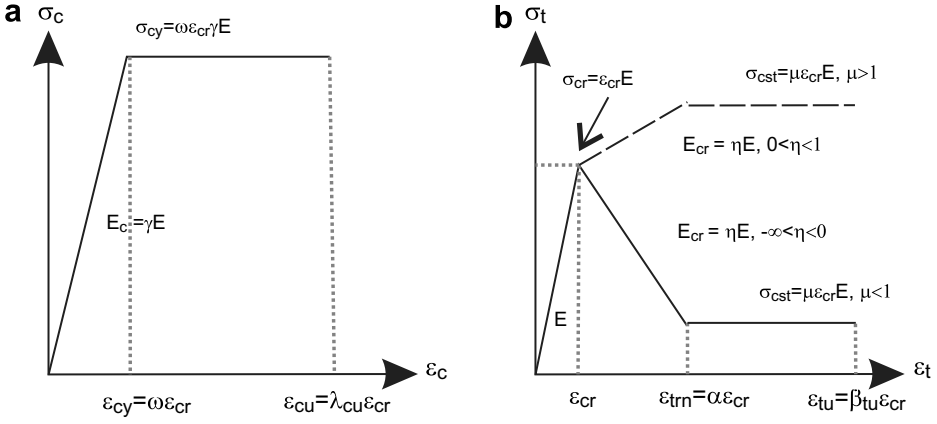


Fig. 2. Material models for homogenized fiber reinforced concrete: (a) compression model and (b) tension model.

solutions for moment–curvature response in non-dimensional forms, the material parameters shown in Fig. 2a and b are defined as a combination of two intrinsic material parameters: the first cracking tensile strain $\varepsilon_{cr}$ and tensile modulus $E$ in addition to seven normalized parameters with respect to $E$ and $\varepsilon_{cr}$ as shown in Eqs. (3)–(5).

$$\omega = \frac{\varepsilon_{cy}}{\varepsilon_{cr}}; \quad \alpha = \frac{\varepsilon_{trn}}{\varepsilon_{cr}}; \quad \beta_{tu} = \frac{\varepsilon_{tu}}{\varepsilon_{cr}}; \quad \lambda_{cu} = \frac{\varepsilon_{cu}}{\varepsilon_{cr}} \tag{3}$$

$$\gamma = \frac{E_c}{E}; \quad \eta = \frac{E_{cr}}{E} \tag{4}$$

$$\mu = \frac{\sigma_{cst}}{E\varepsilon_{cr}} \tag{5}$$

The normalized tensile strain at the bottom fiber $\beta$ and compressive strain at the top fiber $\lambda$ are defined as:

$$\beta = \frac{\varepsilon_{tbot}}{\varepsilon_{cr}}; \quad \lambda = \frac{\varepsilon_{ctop}}{\varepsilon_{cr}} \tag{6}$$

They are linearly related through the normalized neutral axis parameter, $k$.

$$\frac{\lambda\varepsilon_{cr}}{kd} = \frac{\beta\varepsilon_{cr}}{d-kd} \quad \text{or} \quad \lambda = \frac{k}{1-k}\beta \tag{7}$$

Substitution of all normalized parameters defined in Eqs. (3)–(6) into Eqs. (1) and (2) results in the following normalized stress strain models:

$$\frac{\sigma_c(\lambda)}{E\varepsilon_{cr}} = \begin{cases} \gamma\lambda & 0 \leqslant \lambda \leqslant \omega \\ \gamma\omega & \omega < \lambda \leqslant \lambda_{cu} \\ 0 & \lambda_{cu} < \lambda \end{cases}$$

$$\frac{\sigma_t(\beta)}{E\varepsilon_{cr}} = \begin{cases} \beta & 0 \leqslant \beta \leqslant 1 \\ 1+\eta(\beta-1) & 1 < \beta \leqslant \alpha \\ \mu & \alpha < \beta \leqslant \beta_{tu} \\ 0 & \beta_{tu} < \beta \end{cases} \tag{8}$$

In the derivation of moment–curvature diagram for a rectangular cross section with a width $b$ and depth $d$, the Kirchhoff hypothesis of plane section remaining plane for flexural loading is applied. By assuming linear strain distribution across the depth and ignoring shear deformation, the stress–strain relationships in Fig. 2a and b are used to obtain the stress distribution across the cross section as shown in Fig. 3 at three stages of imposed tensile strain: $0 < \beta \leqslant 1$, $1 < \beta \leqslant \alpha$ and $\alpha < \beta \leqslant \beta_{tu}$. For stage 2 and 3 there are two possible scenarios: the compressive strain at top fiber is either elastic ($0 \leqslant \lambda \leqslant \omega$) or plastic ($\omega \leqslant \lambda \leqslant \lambda_{cu}$). These cases will be treated in subsequent sections. Normalized heights of compression and tension zones with respect to beam depth $d$ and the normalized magnitudes of stress at the vertices with respect to the first cracking stress $E\varepsilon_{cr}$ are presented in Tables 1 and 2, respectively. The area and centroid of stress in each zone represent the force components and lines of action. Their normalized values with

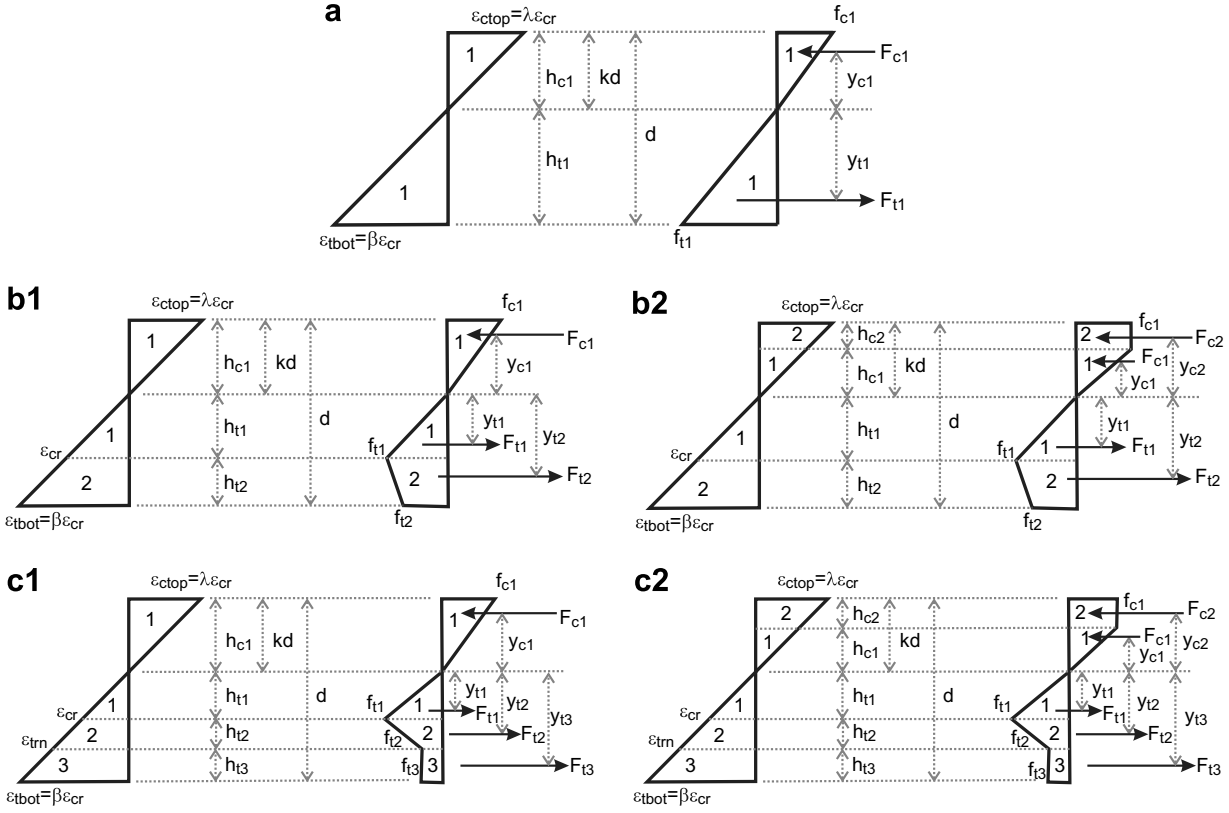


Fig. 3. Stress–strain diagram at different stages of normalized tensile strain at the bottom fiber ($\beta$): (a) $0 \leqslant \beta \leqslant 1$ and $\lambda \leqslant \omega$; (b.1) $1 < \beta \leqslant \alpha$ and $\lambda \leqslant \omega$; (b.2) $1 < \beta \leqslant \alpha$ and $\omega < \lambda \leqslant \lambda_{cu}$; (c.1) $\alpha < \beta \leqslant \beta_{tu}$ and $\lambda \leqslant \omega$; (c.2) $\alpha < \beta \leqslant \beta_{tu}$ and $\omega < \lambda \leqslant \lambda_{cu}$.

Table 1
Normalized height of compression and tension zones for each stage of normalized tensile strain at bottom fiber ($\beta$)

| Normalized height | Stage 1 ($0 \leqslant \beta \leqslant 1$) and ($0 \leqslant \lambda \leqslant \omega$) | Stage 2.1 ($1 < \beta \leqslant \alpha$) and ($0 \leqslant \lambda \leqslant \omega$) | Stage 2.2 ($1 < \beta \leqslant \alpha$) and ($\omega < \lambda \leqslant \lambda_{cu}$) | Stage 3.1 ($\beta > \alpha$) and ($0 \leqslant \lambda \leqslant \omega$) | Stage 3.2 ($\beta > \alpha$) and ($\omega < \lambda \leqslant \lambda_{cu}$) |
|---|---|---|---|---|---|
| $\frac{h_{c2}}{d}$ | – | – | $\frac{k\beta-\omega(1-k)}{\beta}$ | – | $\frac{k\beta-\omega(1-k)}{\beta}$ |
| $\frac{h_{c1}}{d}$ | $k$ | $k$ | $\frac{\omega(1-k)}{\beta}$ | $k$ | $\frac{\omega(1-k)}{\beta}$ |
| $\frac{h_{t1}}{d}$ | $1-k$ | $\frac{1-k}{\beta}$ | $\frac{1-k}{\beta}$ | $\frac{1-k}{\beta}$ | $\frac{1-k}{\beta}$ |
| $\frac{h_{t2}}{d}$ | – | $\frac{(1-k)(\beta-1)}{\beta}$ | $\frac{(1-k)(\beta-1)}{\beta}$ | $\frac{(1-k)(\alpha-1)}{\beta}$ | $\frac{(1-k)(\alpha-1)}{\beta}$ |
| $\frac{h_{t3}}{d}$ | – | – | – | $\frac{(1-k)(\beta-\alpha)}{\beta}$ | $\frac{(1-k)(\beta-\alpha)}{\beta}$ |

Table 2
Normalized stress at vertices in the stress diagram for each stage of normalized tensile strain at bottom fiber ($\beta$)

| Normalized stress | Stage 1 ($0 \leqslant \beta \leqslant 1$) and ($0 \leqslant \lambda \leqslant \omega$) | Stage 2.1 ($1 < \beta \leqslant \alpha$) and ($0 \leqslant \lambda \leqslant \omega$) | Stage 2.2 ($1 < \beta \leqslant \alpha$) and ($\omega < \lambda \leqslant \lambda_{cu}$) | Stage 3.1 ($\beta > \alpha$) and ($0 \leqslant \lambda \leqslant \omega$) | Stage 3.2 ($\beta > \alpha$) and ($\omega < \lambda \leqslant \lambda_{cu}$) |
|---|---|---|---|---|---|
| $\frac{f_{c2}}{E\varepsilon_{cr}}$ | – | – | $\omega\gamma$ | – | $\omega\gamma$ |
| $\frac{f_{c1}}{E\varepsilon_{cr}}$ | $\frac{\gamma\beta k}{1-k}$ | $\frac{\gamma\beta k}{1-k}$ | $\omega\gamma$ | $\frac{\gamma\beta k}{1-k}$ | $\omega\gamma$ |
| $\frac{f_{t1}}{E\varepsilon_{cr}}$ | $\beta$ | 1 | 1 | 1 | 1 |
| $\frac{f_{t2}}{E\varepsilon_{cr}}$ | – | $1+\eta(\beta-1)$ | $1+\eta(\beta-1)$ | $1+\eta(\alpha-1)$ | $1+\eta(\alpha-1)$ |
| $\frac{f_{t3}}{E\varepsilon_{cr}}$ | – | – | – | $\mu$ | $\mu$ |

Table 3
Normalized force component for each stage of normalized tensile strain at bottom fiber ($\beta$)

| Normalized force component | Stage 1 ($0 \leqslant \beta \leqslant 1$) and ($0 \leqslant \lambda \leqslant \omega$) | Stage 2.1 ($1 < \beta \leqslant \alpha$) and ($0 \leqslant \lambda \leqslant \omega$) | Stage 2.2 ($1 < \beta \leqslant \alpha$) and ($\omega < \lambda \leqslant \lambda_{cu}$) | Stage 3.1 ($\beta > \alpha$) and ($0 \leqslant \lambda \leqslant \omega$) | Stage 3.2 ($\beta > \alpha$) and ($\omega < \lambda \leqslant \lambda_{cu}$) |
|---|---|---|---|---|---|
| $\frac{F_{c2}}{bdE\varepsilon_{cr}}$ | – | – | $\frac{\omega\gamma}{\beta}(\beta k+\omega k-\omega)$ | – | $\frac{\omega\gamma}{\beta}(\beta k+\omega k-\omega)$ |
| $\frac{F_{c1}}{bdE\varepsilon_{cr}}$ | $\frac{\beta\gamma k^2}{2(1-k)}$ | $\frac{\beta\gamma k^2}{2(1-k)}$ | $\frac{\omega^2\gamma}{2\beta}(1-k)$ | $\frac{\beta\gamma k^2}{2(1-k)}$ | $\frac{\omega^2\gamma}{2\beta}(1-k)$ |
| $\frac{F_{t1}}{bdE\varepsilon_{cr}}$ | $\frac{\beta}{2}(1-k)$ | $\frac{(1-k)}{2\beta}$ | $\frac{(1-k)}{2\beta}$ | $\frac{(1-k)}{2\beta}$ | $\frac{(1-k)}{2\beta}$ |
| $\frac{F_{t2}}{bdE\varepsilon_{cr}}$ | – | $\frac{(1-k)(\beta-1)(\eta\beta-\eta+2)}{2\beta}$ | $\frac{(1-k)(\beta-1)(\eta\beta-\eta+2)}{2\beta}$ | $\frac{(1-k)(\alpha-1)(\eta\alpha-\eta+2)}{2\beta}$ | $\frac{(1-k)(\alpha-1)(\eta\alpha-\eta+2)}{2\beta}$ |
| $\frac{F_{t3}}{bdE\varepsilon_{cr}}$ | – | – | – | $\frac{(1-k)(\beta-\alpha)\mu}{\beta}$ | $\frac{(1-k)(\beta-\alpha)\mu}{\beta}$ |

Table 4
Normalized moment arm of force component for each stage of normalized tensile strain at bottom fiber ($\beta$)

| Normalized moment arm | Stage 1 ($0 \leqslant \beta \leqslant 1$) and ($0 \leqslant \lambda \leqslant \omega$) | Stage 2.1 ($1 < \beta \leqslant \alpha$) and ($0 \leqslant \lambda \leqslant \omega$) | Stage 2.2 ($1 < \beta \leqslant \alpha$) and ($\omega < \lambda \leqslant \lambda_{cu}$) | Stage 3.1 ($\beta > \alpha$) and ($0 \leqslant \lambda \leqslant \omega$) | Stage 3.2 ($\beta > \alpha$) and ($\omega < \lambda \leqslant \lambda_{cu}$) |
|---|---|---|---|---|---|
| $\frac{y_{c2}}{d}$ | – | – | $\frac{\beta k+\omega(1-k)}{2\beta}$ | – | $\frac{\beta k+\omega(1-k)}{2\beta}$ |
| $\frac{y_{c1}}{d}$ | $\frac{2}{3}k$ | $\frac{2}{3}k$ | $\frac{2}{3}\frac{\omega(1-k)}{\beta}$ | $\frac{2}{3}k$ | $\frac{2}{3}\frac{\omega(1-k)}{\beta}$ |
| $\frac{y_{t1}}{d}$ | $\frac{2}{3}(1-k)$ | $\frac{2}{3}\frac{(1-k)}{\beta}$ | | $\frac{2}{3}\frac{(1-k)}{\beta}$ | |
| $\frac{y_{t2}}{d}$ | – | $\frac{2\eta\beta^2-\eta\beta-\eta+3\beta+3}{3\beta(\eta\beta-\eta+2)}(1-k)$ | | $\frac{2\eta\alpha^2-\eta\alpha-\eta+3\alpha+3}{3\beta(\eta\alpha-\eta+2)}(1-k)$ | |
| $\frac{y_{t3}}{d}$ | – | – | – | $\frac{(\alpha+\beta)}{2\beta}(1-k)$ | |

respect to cracking tensile force $bdE\varepsilon_{cr}$ and beam depth $d$ are presented in Tables 3 and 4, respectively.

Table 5 shows the steps in determination of net section force, moment, and curvature at each stage of applied tensile strain, $\beta$. The net force is obtained as the difference between the tension and compression forces, equated to zero for internal equilibrium, and solved for the neutral axis depth ratio $k$. The expressions for net force in stage 2 and 3 are in the quadratic forms and result in two solutions for $k$. With a large scale of numerical tests covering a practical range of material parameters, only one solution of $k$ yields the valid value in the range $0 < k < 1$ and it is presented in Table 6. The internal moment is obtained by operating on the force components and their distance from

Table 5
Equilibrium of force, moment and curvature for each stage of normalized tensile strain at bottom fiber ($\beta$)

| Stage | Tension | Compression | Force equilibrium | Internal moment |
|---|---|---|---|---|
| 1 | $0 \leqslant \beta \leqslant 1$ | $0 \leqslant \lambda \leqslant \omega$ | $-F_{c1} + F_{t1}$ | $F_{c1}y_{c1} + F_{t1}y_{t1}$ |
| 2.1 | $1 < \beta \leqslant \alpha$ | $0 \leqslant \lambda \leqslant \omega$ | $-F_{c1} + F_{t1} + F_{t2}$ | $F_{c1}y_{c1} + F_{t1}y_{t1} + F_{t2}y_{t2}$ |
| 2.2 | $1 < \beta \leqslant \alpha$ | $\omega < \lambda \leqslant \lambda_{cu}$ | $-F_{c1} - F_{c2} + F_{t1} + F_{t2}$ | $F_{c1}y_{c1} + F_{c2}y_{c2} + F_{t1}y_{t1} + F_{t2}y_{t2}$ |
| 3.1 | $\beta > \alpha$ | $0 \leqslant \lambda \leqslant \omega$ | $-F_{c1} + F_{t1} + F_{t2} + F_{t3}$ | $F_{c1}y_{c1} + F_{t1}y_{t1} + F_{t2}y_{t2} + F_{t3}y_{t3}$ |
| 3.2 | $\beta > \alpha$ | $\omega < \lambda \leqslant \lambda_{cu}$ | $-F_{c1} - F_{c2} + F_{t1} + F_{t2} + F_{t3}$ | $F_{c1}y_{c1} + F_{c2}y_{c2} + F_{t1}y_{t1} + F_{t2}y_{t2} + F_{t3}y_{t3}$ |

Note that curvature $= \varepsilon_c/(kd)$.

Table 6
Neutral axis depth ratio, normalized moment and curvature for each stage of normalized tensile strain at bottom fiber ($\beta$)

| Stage | $k$ | $M'$ | $\phi'$ |
|---|---|---|---|
| 1 | $k_1 = \begin{cases} \frac{1}{2} & \text{for } \gamma = 1 \\ \frac{-1+\sqrt{\gamma}}{-1+\gamma} & \text{for } \gamma < 1 \text{ or } \gamma > 1 \end{cases}$ | $M'_1 = \frac{2\beta[(\gamma-)k_1^3+3k_1^2-3k_1+1]}{1-k_1}$ | $\phi'_1 = \frac{\beta}{2(1-k_1)}$ |
| 2.1 | $k_{21} = \frac{\beta^2\gamma+D_{21}-\sqrt{\gamma^2\beta^4+D_{21}\gamma\beta^2}}{D_{21}}$<br>$D_{21} = \eta(\beta^2 - 2\beta + 1) + 2\beta - \beta^2\gamma - 1$ | $M'_{21} = \frac{(2\beta\gamma+C_{21})k_{21}^3-3C_{21}k_{21}^2+3C_{21}k_{21}-C_{21}}{1-k_{21}}$<br>$C_{21} = \frac{-2\eta\beta^3+3\eta\beta^2-3\beta^2-\eta+1}{\beta^2}$ | $\phi'_{21} = \frac{\beta}{2(1-k_{21})}$ |
| 2.2 | $k_{22} = \frac{D_{22}}{D_{22}+2\omega\gamma\beta}$<br>$D_{22} = \eta(\beta^2 - 2\beta + 1) + 2\beta + \omega^2\gamma - 1$ | $M'_{22} = (3\omega\gamma + C_{22})k_{22}^2 - 2C_{22}k_{22} + C_{22}$<br>$C_{22} = \frac{2\eta\beta^3-3\eta\beta^2+3\beta^2-\omega^3\gamma+\eta-1}{\beta^2}$ | $\phi'_{22} = \frac{\beta}{2(1-k_{22})}$ |
| 3.1 | $k_{31} = \frac{D_{31}-\sqrt{\gamma\beta^2D_{31}}}{D_{31}-\beta^2\gamma}$<br>$D_{31} = \eta(\alpha^2 - 2\alpha + 1) + 2\mu(\beta - \alpha) + 2\alpha - 1$ | $M'_{31} = \frac{(C_{31}-2\beta\gamma)k_{31}^3-3C_{31}k_{31}^2+3C_{31}k_{31}-C_{31}}{k_{31}-1}$<br>$C_{31} = \frac{3(\mu\beta^2-\mu\alpha^2-\eta\alpha^2+\alpha^2)+2\eta\alpha^3+\eta-1}{\beta^2}$ | $\phi'_{31} = \frac{\beta}{2(1-k_{31})}$ |
| 3.2 | $k_{32} = \frac{D_{32}}{D_{32}+2\omega\gamma\beta}$<br>$D_{32} = \omega^2\gamma + \eta\alpha^2 + 2(\mu\beta - \eta\alpha - \mu\alpha + \alpha) + \eta - 1$ | $M'_{32} = (C_{32} + 3\omega\gamma)k_{32}^2 - 2C_{32}k_{32} + C_{32}$<br>$C_{32} = \frac{3(\mu\beta^2-\mu\alpha^2-\eta\alpha^2+\alpha^2)+2\eta\alpha^3-\omega^3\gamma+\eta-1}{\beta^2}$ | $\phi'_{32} = \frac{\beta}{2(1-k_{32})}$ |

the neutral axis and the curvature is determined as the ratio of compressive strain at top fiber ($\varepsilon_{ctop} = \lambda\varepsilon_{cr}$) to the depth of neutral axis $kd$. The moment $M_i$ and curvature $\phi_i$ at each stage $i$ are then normalized with respect to the values at cracking $M_{cr}$ and $\phi_{cr}$, respectively and their closed form solutions are presented in Table 6.

$$M_i = M'_i M_{cr}; \quad M_{cr} = \frac{1}{6}bd^2E\varepsilon_{cr} \tag{9}$$

$$\phi_i = \phi'_i\phi_{cr}; \quad \phi_{cr} = \frac{2\varepsilon_{cr}}{d} \tag{10}$$

As mentioned earlier, the compressive strain at the top fiber $\lambda$ in stage 2 or 3 could be either in elastic ($0 \leqslant \lambda \leqslant \omega$) or plastic ($\omega < \lambda \leqslant \lambda_{cu}$) range, depending on the applied tensile strain $\beta$ and neutral axis parameter $k$. The range can be identified by assuming $\lambda < \omega$ [Fig. 3(b.1) or (c.1)] and using the expression $k_{21}$ or $k_{31}$ in Table 6 to determine $\lambda$ from Eq. (7). If $\lambda < \omega$ holds true, the assumption is correct, otherwise $\lambda > \omega$ and the expression $k_{22}$ or $k_{32}$ is used instead. Once, the neutral axis parameter $k$ and the applicable case are determined, the appropriate expressions for moment and curvature in Table 6 and Eqs. (9) and (10) are used.

## 3. Crack localization rules

When a flexural specimen is loaded beyond the peak strength, the load decreases and two distinct zones develop as the deformation localizes in the cracking region while the remainder of the specimen undergoes general unloading. To correlate the stress-crack width relationship into the stress–strain approach, localization of major cracks is simulated as an average response over the crack spacing region. Results are used as a smeared crack in conjunction with the moment–curvature diagram to obtain load deformation behavior.

Fig. 4a presents the schematic moment–curvature diagram with crack localization rules and Fig. 4b shows a four point bending test with localization of smeared crack occurs in the mid-zone; while the zones outside the cracking region undergo unloading during softening [25,26]. The length of the localized zone is defined as "$cS$" representing product of a normalized parameter $c$ and loading point spacing $S = L/3$, where $L$ is the clear span. For the simulations of fiber reinforced composites in this paper, it was assumed that cracks were uniformly distributed throughout the mid-zone and a value of $c = 0.5$ was used.

Moment distribution along the length of a beam is obtained by static equilibrium and the corresponding curvature is obtained from a moment–curvature relationship. As shown by a solid curve in Fig. 4a, a typical moment–curvature diagram is divided into two portions: an ascending curve from 0 to $M_{max}$ and a descending curve from $M_{max}$ to $M_{fail}$. For a special case of low-fiber volume fraction where an ascending curve from 0 to $M_{max1}$, representing the tensile cracking strength is followed by a sharp drop

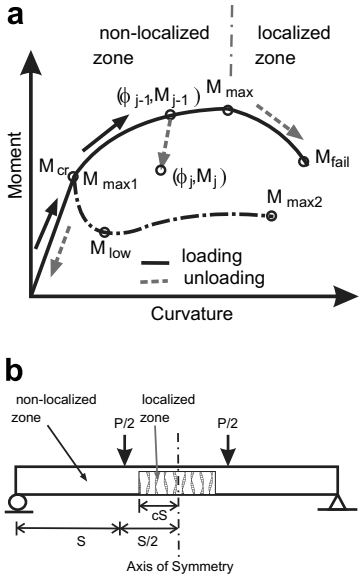


Fig. 4. (a) Moment–curvature diagram and crack localization rules and (b) four point bending test.

in the post-peak response, the post-peak moment–curvature response exhibits two portions: a descending curve from $M_{max1}$ to $M_{low}$ and ascending again from $M_{low}$ to $M_{max2}$. In this case, there are two local maxima, which either point could be the global maximum.

To predict load–deflection response, static equilibrium is used and an array of load steps is derived from a series of discrete data points along a moment–curvature diagram. For each load step, the moment and corresponding curvature distribution along the beam are calculated. While the specimen is loaded from 0 to $M_{max}$ (or $M_{max1}$), the ascending portion of the diagram is used. Beyond the maximum load, as the specimen undergoes softening, the curvature distribution depends on the localized or non-localized zones and its prior strain history (uncracked or cracked). For an uncracked section, the curvature unloads elastically. If the section has been loaded beyond $M_{cr}$, the unloading curvature of cracked sections follows a quasi-linear recovery path expressed as:

$$\phi_j = \phi_{j-1} - \xi \frac{(M_{j-1} - M_j)}{EI} \tag{11}$$

where $\phi_{j-1}$ and $M_{j-1}$ represent the previous moment–curvature state and $\phi_j$, and $M_j$ are the current state. $E$ and $I$ represent the elastic modulus and the moment of inertia of uncracked section. The unloading factor $\xi$ is between 0 and 1; $\xi = 0$ indicates no curvature recovery while $\xi = 1$ is unloading elastically with initial stiffness $EI$. An unloading factor $\xi = 0$ was used in the present study under the assumption that cracks do not close when material softens in displacement control. For a section in the localized zone, the unloading curvature is determined from the descending portion of the moment–curvature diagram ($M_{max}$ to $M_{fail}$) or ($M_{max1}$ to $M_{low}$). For a special case of low-fiber content that the moment–curvature diagram is divided into three portions, the curvature corresponding to the load step beyond the $M_{low}$ is determined by the third portion ($M_{low}$ to $M_{max2}$).

## 4. Algorithm to predict load–deflection response of four point bending test

The load–deflection response of a beam can be obtained by using the moment–curvature response, crack localization rules, and moment-area method as follows.

(1) For a given cross section and material properties, the normalized tensile strain at the bottom fiber $\beta$ is incrementally imposed to generate the moment–curvature response using Eqs. (9), (10), and the expressions given in Table 6. For each value of $\beta$ in stage 2 and 3, the condition for compressive stress $\lambda < \omega$ or $\lambda > \omega$ is verified in advance of moment–curvature calculation.
(2) Since a moment–curvature diagram determines the maximum load allowed on a beam section, the discrete moments along the diagram are used to calculate the applied load vector $P = 2M/S$ as shown in Fig. 4.
(3) The beam is segmented into finite sections. For a given load step, use static equilibrium to calculate moment distribution along the beam and use moment–curvature relationship with crack localization rules to identify the curvature.
(4) The deflection at mid-span is calculated by numerical moment-area method of discrete curvature between the support and mid-span. This procedure is applied at each load step to until a complete load–deflection response is obtained. A simplified procedure for direct calculation of the deflection is presented in an earlier work [24].

## 5. Parametric study of material parameters

Two sets of parametric studies were conducted to address the behavior of strain softening and strain hardening materials. The flexural strength and ductility for each material parameter studied were expressed as the normalized moment–curvature response, which is independent of section size and first cracking tensile strength.

Fig. 5 presents the parametric study of a typical strain softening material with material parameters specified as a compressive to tensile strength ratio $\gamma\omega = 10$, normalized ultimate compressive strain $\lambda_{cu} = 30$ and ultimate tensile strain $\beta_{tu} = 150$. For each case of study, all parameters were held constant to the typical values while the parameters subjected to study were varied. In order to avoid a discontinuous tensile response at the transition strain $\alpha$ for strain softening materials, the post-peak modulus $\eta$ is determined by Eq. (12)

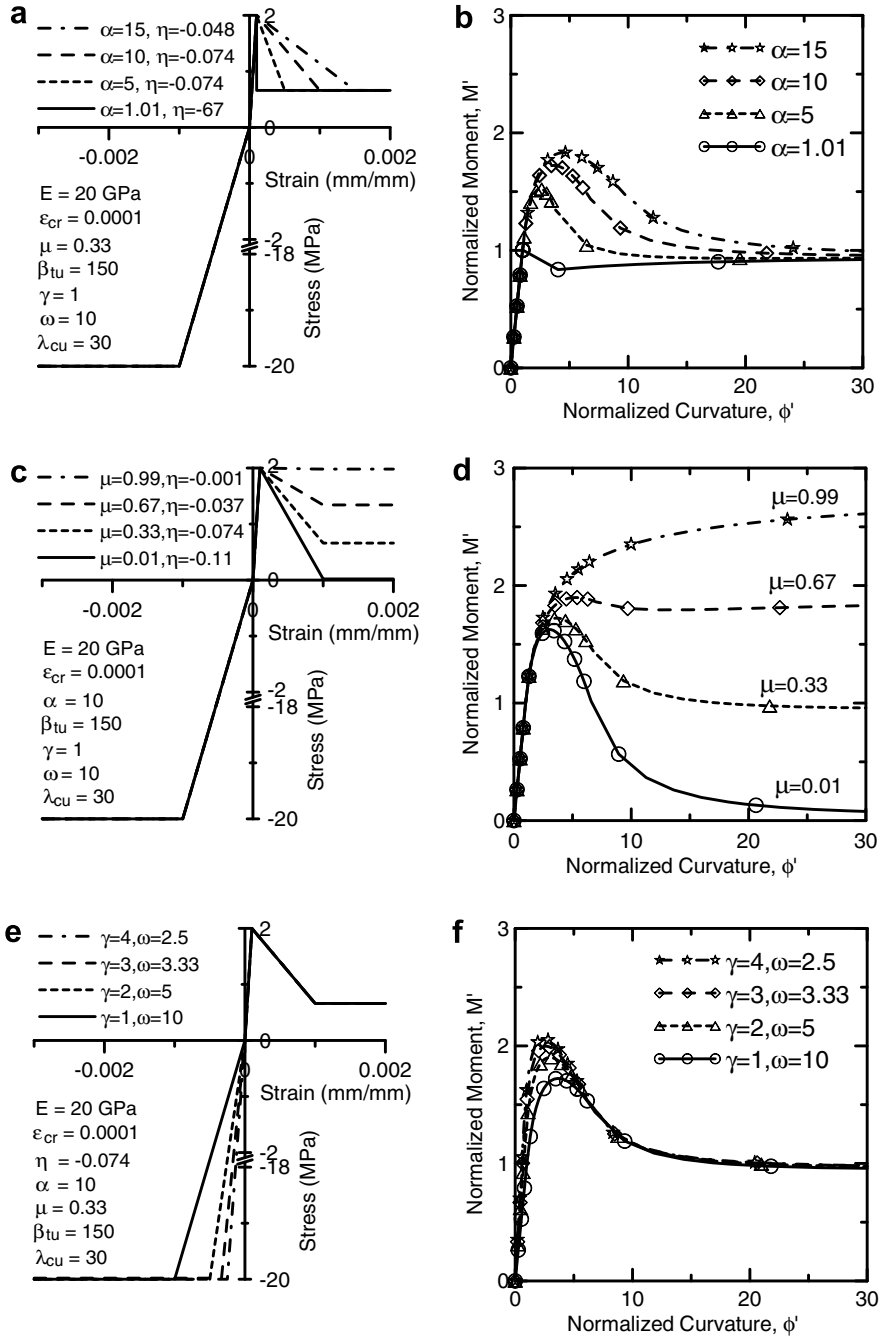


Fig. 5. Parametric study of a typical strain softening material: the effect of parameters $\alpha$, $\mu$ and $\gamma$ & $\omega$ to normalized moment–curvature diagram.

$$\eta = -\frac{(1-\mu)}{(\alpha-1)} \tag{12}$$

Fig. 5a depicts the compression and tension model with the transition strain $\alpha$ varied from 1.01 to 15. Fig. 5b reveals that an increase in the transition strain $\alpha$, increases both flexural strength and ductility. Fig. 5c depicts the material model with the residual tensile strength $\mu$ varied from 0.01 to 0.99, simulating a range of brittle concrete to elastic–perfectly plastic response of high volume fraction fiber reinforced concrete. Fig. 5d shows that moment–curvature diagram is quite sensitive to the variations in parameter $\mu$ as it significantly affects the peak and post-peak response. The flexural response changes from a brittle to ductile material as $\mu$ changes from 0.01 to 0.99. In order to study the effect of compressive stiffness, the range of parameters $\gamma$ and $\omega$ were used together to represent the increase in relative compressive to tensile stiffness from $0.1 < \gamma/\omega < 16$ (1/10 to 4/2.5) at a fixed compressive to tensile strength ratio ($\gamma\omega = 10$) as shown in Fig. 5e. Fig. 5f reveals that the changes in the relative stiffness slightly affect the peak moment from 1.7 to 2.1 and marginally increases the stiffness of the moment–curvature response. It is also concluded that the normalized compressive modulus $\gamma$ and

compressive yield strain $\omega$ have a marginal effect on the predicted moment–curvature response as long as the compressive strength is about one order of magnitude higher than the first cracking tensile strength.

Fig. 6 presents the parametric study of a typical strain hardening material, with a compressive to tensile cracking strength ratio of $\gamma\omega = 10$, normalized ultimate compressive strain $\lambda_{cu} = 30$ and ultimate tensile strain $\beta_{tu} = 150$ similar to the previous case study. The post-peak response was ignored for this case by setting $\mu$ to a very low value of 0.01. Fig. 6a shows the compression and tension model of a typical strain hardening material with varying $\alpha = 1.01$–15. Fig. 6b shows that the increase in $\alpha$ directly increases the normalized moment and curvature. Fig. 6c and d demonstrate that increasing the post-crack modulus $\eta$ also significantly increases the moment–curvature diagram. Similar to the strain softening materials, the increase in relative compressive to tensile stiffness at constant compressive to tensile strength ratio $\gamma\omega$ (as shown in Fig. 6e) has a subtle effect to the moment–curvature response as shown in Fig. 6f. These results indicate that the most significant parameters affecting the moment capacity are the transition strain $\alpha$ and the stiffness in the post-cracking tensile range $\eta$.

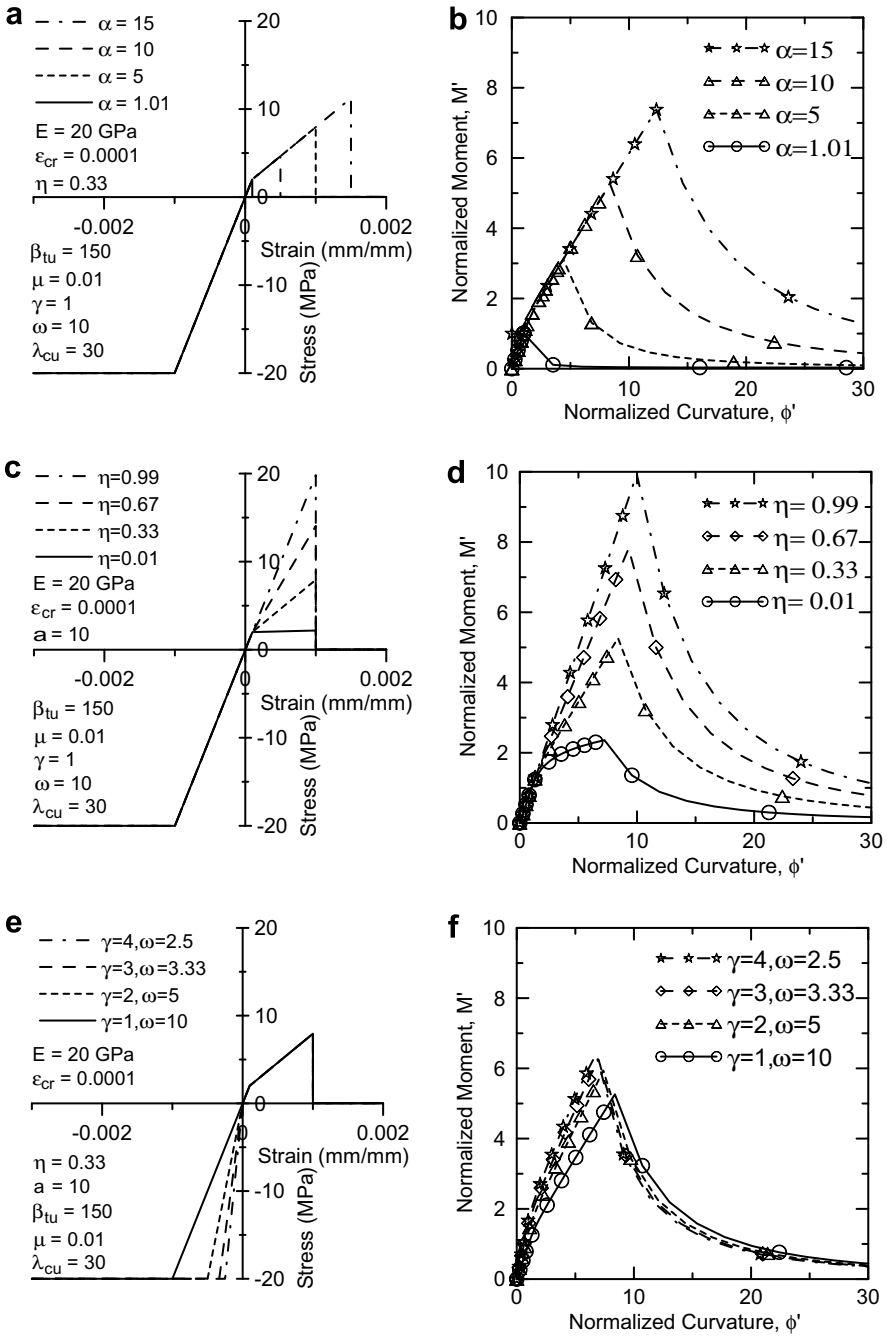


Fig. 6. Parametric study of a typical strain hardening material: the effect of parameters $\alpha$, $\eta$ and $\gamma$ and $\omega$ to normalized moment–curvature diagram.

## 6. Prediction of load deformation response

The algorithm to simulate load–deflection response of a beam under four point bending test was used as a predictive tool to study three classes of materials: SFRC with 0.5% and 1.0% volume fraction representing strain softening–deflection softening and deflection hardening materials, respectively, and ECC with 2.0% volume fraction representing strain hardening material.

### 6.1. Simulation of Steel Fiber Reinforced Concrete (SFRC)

Two mixes of SFRC (H1 and H21) that used hook-end fibers at volume fraction levels of 0.5% and 1.0% were selected from the literature [7,8] to demonstrate the algorithm to predict load–deflection responses. Tensile "dog bone" specimens of $100 \times 70 \times 200$ mm in net dimensions with an enlarged width of 100 mm at the ends were used. The flexural four point bending specimens were $100 \times 100 \times 1000$ mm with a clear span of 750 mm. The average material properties were: compressive strength $f'_c = 34$ MPa, initial compressive modulus $E_{ci} = 28.5$ GPa and initial tensile modulus $E = 25.4$ GPa. The first cracking tensile strain $\varepsilon_{cr}$ for mix H1 and H21 are 110.6 and 116.2 microstrains, respectively.

As shown in the parametric studies, the material parameters for compression model have a marginal effect to the predicted flexural response as long as the compressive strength is as much nine times greater than the tensile strength [24]. Therefore, typical values for compression parameters can be estimated without severely affecting the results. The compressive yield stress $f_{cy}$ was assumed to be $0.85fc'$ and compressive modulus $E_c$ was estimated to be $0.85E_{ci}$. The normalized compressive modulus $\gamma$ was then obtained by $E_c/E$ and the normalized compressive yield strain by $\omega = f_{cy}/(E_c\varepsilon_{cr})$. The range of ultimate compressive strain $\varepsilon_{cu}$ between 0.0035 and 0.004 was suggested by several researchers [27,28]. The value of 0.004 was selected in this study and the corresponding normalized value was calculated by $\lambda_{cu} = \varepsilon_{cu}/\varepsilon_{cr}$. The material parameters for tension model were determined by fitting the model to the uniaxial tension test result as shown by the solid line in Fig. 7a and c. All other parameters used in the simulation of flexural bending of mix H1 and H21 are provided in the figures.

For deflection-softening material represented by mix H1, the constant post-peak stress level $\mu = 0.24$, post-crack stiffness $\eta = -0.76$, post crack stiffness ultimate strain capacity $\alpha = 2.0$, total tensile strain level $\beta_{tu} = 136$, compression to tension stiffness ratio $\gamma = 0.95$ and compression

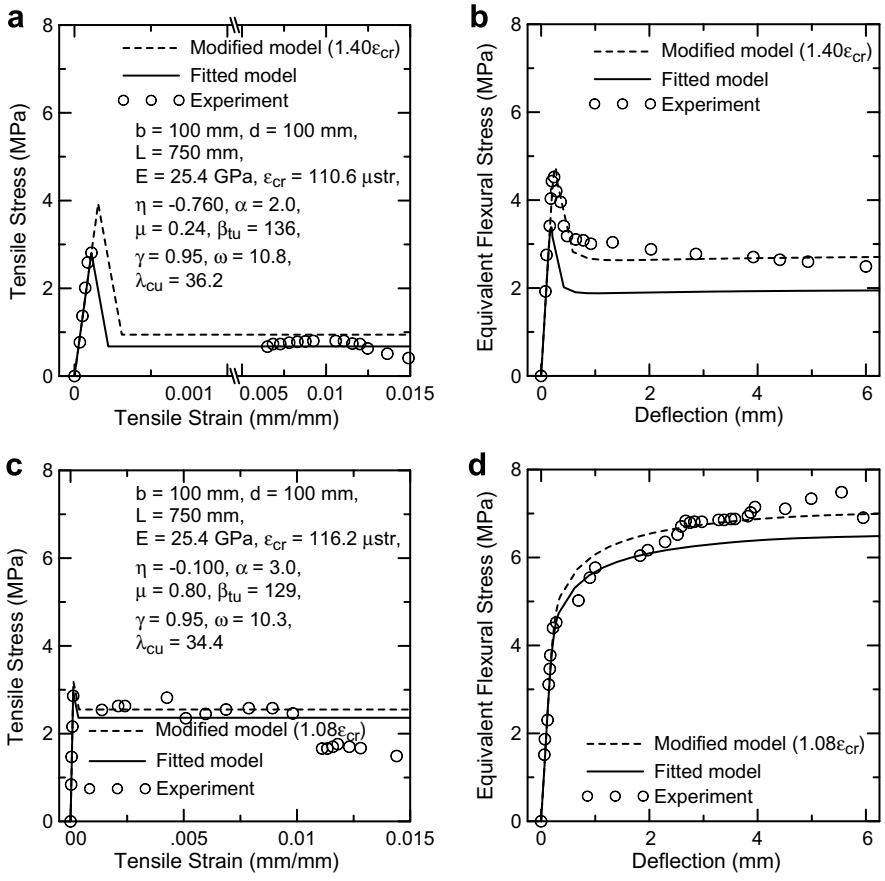


Fig. 7. Simulation of a Steel Fiber Reinforced Concrete (SFRC): (a and b) tension model and flexural response of mix H1 ($V_f = 0.5\%$); (c and d) tension model and flexural response of mix H21 ($V_f = 1.0\%$).

to tension strength ratio of $\omega = 10.8$ were used. The solid curve in Fig. 7b shows the predicted flexural response of deflection softening material (mix H1) from the simulation process. It is shown that use of uniaxial tension data underpredicts the flexural response for this class of material. This is attributed to differences in the stress distribution profiles of the two test methods. In the tension test, the entire volume of the specimen is a potential zone for crack initiation. Comparatively, in the flexural test, only a small fraction of the tension region is subjected to an equivalent ultimate tensile stress. To quantify the differences between the equivalent tensile strengths of tension and flexure, the authors propose a single scaling parameter. By using a multiplier that is applied to the first cracking tensile strain $\varepsilon_{cr}$, associated strains and stresses increase by the same scale, resulting in a uniform increase in material strength. An inverse analysis by trial and error was conducted to identify the appropriate scaling parameter for this case and it found that the material model should be scaled up uniformly by 40%. The dash lines in Fig. 7a and b show the modified strength and the new prediction, which provides a better match to the experimental results. If tensile and flexural responses of several samples are utilized, the inverse analysis procedure can be used to establish the statistical relationship between the tensile and flexural responses as have been done for other brittle materials [29].

For deflection-hardening materials represented by mix H21, the solid curve of tension model that fits to the uniaxial tension test data are shown in Fig. 7c. The constant post-peak stress level $\mu = 0.8$, post-crack stiffness $\eta = -0.1$, transition strain $\alpha = 3.0$, ultimate tensile strain level $\beta_{tu} = 129$, compression to tension stiffness ratio $\gamma = 0.95$ and compressive yield strain to first cracking tensile strain ratio of $\omega = 10.3$ were used. The predicted flexural response is shown as a solid line in Fig. 7d. The algorithm slightly underestimates the flexural response. The inverse analysis found that the strength of the uniaxial models should be increased by 8% for a reasonable prediction of flexural results as shown by the dashed lines in Fig. 7c and d. Note that the correlation of experimental and simulated responses in the deflection hardening range is quite reasonable; the discrepancy between the fitted and modified tension models is much lower than that of strain softening materials. This indicates that for the deflection hardening materials, the model predictions are quite reasonable.

### 6.2. Simulation of Engineered Cementitious Composite (ECC)

An ECC mix that used polyethylene fibers at volume fraction levels of 2.0% from the literature [14,15] was selected to demonstrate the ability of the algorithm to predict load–deflection response for strain hardening material. The flexural specimens for the four point bending test were $76.2 \times 101.6 \times 355.6$ mm with a clear span of 304.8 mm. The average material properties were: compressive strength $f'_c = 60$ MPa. The initial compressive modulus $E_{ci} = 4.35$ GPa was obtained by back-calculation of the initial flexural load–deflection response. The initial tensile modulus $E = 4.75$ GPa and the first cracking tensile strain $\varepsilon_{cr} = 600$ microstrains were obtained directly from the uniaxial tensile test results. The constant post-peak stress level $\mu = 1.49$, post-crack stiffness $\eta = 0.009$, post-crack strain capacity $\alpha = 95.0$, ultimate tensile strain level $\beta_{tu} = 117$, compression to tension stiffness ratio $\gamma = 0.92$ and compressive yield strain to first cracking tensile strain ratio of $\omega = 18.4$ were used.

The compressive yield stress $f_{cy}$ was assumed to be $0.80fc'$ and compressive modulus $E_c$ was estimated equal to $E_{ci}$. The ultimate compressive strain $\varepsilon_{cu}$ was assumed to be 0.012. The material parameters for tension model were determined by fitting the model to the uniaxial tension test result as shown by the solid line in Fig. 8a. All parameters used in the simulation are provided in the same figure. The solid curve in Fig. 8b shows the predicted flexural response obtained by the simulation process. The prediction for the strain hardening material during the pre- and post-crack stages agreed well with the experimental results; note that the formation of the distributed crack system can

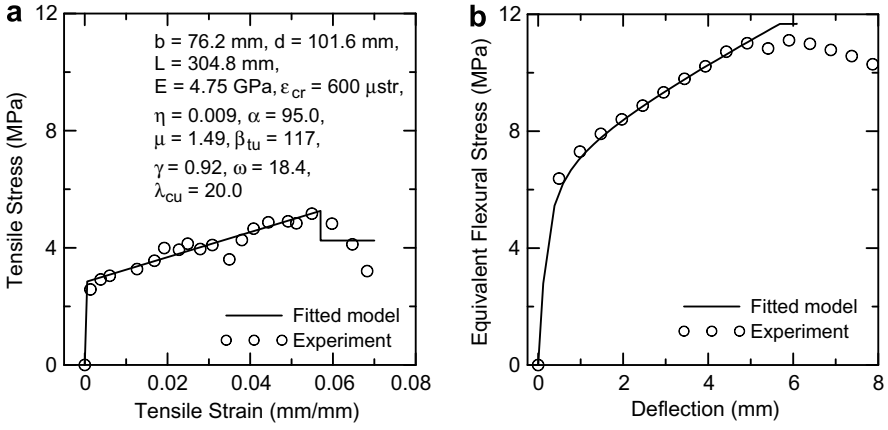


Fig. 8. Simulation of Engineered Cementitious Composite (ECC): (a) tension model and (b) flexural response.

be adequately described by the smeared pseudo-strain model.

## 7. Discussion

The three simulations of fiber reinforced concrete materials, ranging from low to high fiber contents and material response changing from softening to hardening, indicate that as the post-peak tensile strength of material increases, the use of uniaxial response to predict flexural response becomes more accurate. It also implies that the increase of fiber contents in the experiments can effectively suppress the flaws from initiating crack that leads to premature failure, especially under uniaxial tensile conditions. Therefore, the flaw size distribution in material is less sensitive to the constant vs. linear distribution of tensile stress patterns in uniaxial and flexural specimens, respectively.

## 8. Conclusions

This paper presents closed form solutions for generating moment–curvature diagrams of a rectangular beam made of homogenized fiber reinforced concrete. The algorithm using a moment–curvature diagram with crack localization rules and moment-area method to predict load deformation of a beam under the four point bending test was also developed. The normalized moment–curvature diagram obtained by closed form solutions were used in parametric studies of strain softening and strain hardening materials. For a typical strain softening material, the most important factors to flexural strength and ductility are the constant residual tensile strength and the strain at ultimate tensile strength. For a typical strain hardening material, both tensile strain at transition and post-crack modulus are almost equally important to the flexural behavior of a beam. Strain softening and hardening materials share the similarity that the change of relative compressive to tensile stiffness slightly affects the flexural response as long as the compressive to tensile strength ratio is greater than 9.

Load–deflection responses of four point bending tests revealed that the use of uniaxial tensile data tends to under-predict the flexural response for the material that has a relatively low post-crack tensile strength. This was in part due to a difference in stress distribution between the uniaxial tension and bending tests. The under-predicted load deformation response can be corrected by increasing strength of the uniaxial material model using a scaling parameter to the first cracking strain. With this approach, other associated strains and stresses will subsequently be increased by the same factor. With proper scaling parameters, the predicted responses agree well with experimental observations. It is also observed that as fiber content, or bond is increased such that the post-crack tensile strength is improved, the size effect observed in predicting the response of flexural samples tends to be reduced and the use of uniaxial response to predict flexural response becomes more accurate.

## Acknowledgement

The authors acknowledge financial support of the National Science Foundation, Program 0324669-03 under Dr. P. Balaguru.

## References

[1] Mobasher B, Shah SP. Test parameters for evaluating toughness of glass fiber reinforced concrete panels. ACI Mater J 1989;86(5):448–58.
[2] Mobasher B, Li CY. Mechanical properties of hybrid cement-based composites. ACI Mater J 1996;93(3):284–92.
[3] Romualdi JP, Batson GB. Mechanics of crack arrest in concrete. Proc ASCE 1963;89(3):147–68.
[4] Majumdar AJ, Laws V. Composite materials based on cement matrices. Philos Trans R Soc Lond Ser A: Math Phys Sci 1983:191–202.
[5] Mobasher B, Li CY. Effect of interfacial properties on the crack propagation in cementitious composites. Adv Cement Based Mater 1996;4(3–4):93–105.
[6] Umekawa S, Nakazawa K. On mechanical properties of stainless steel fiber and fiber-reinforced stainless-SN–PB alloy composite. J Jap Inst Metals 1970;34(2):222–7.
[7] Lim TY, Paramasivam P, Lee SL. Analytical model for tensile behavior of steel–fiber concrete. ACI Mater J 1987;84(4):286–98.
[8] Lim TY, Paramasivam P, Lee SL. Bending behavior of steel–fiber concrete beams. ACI Struct J 1987;84(6):524–36.
[9] Glass Fiber Reinforced Concrete (GFRC). PCI Committee on glass fiber reinforced concrete panels. 3rd ed.; 1993.
[10] Krstulovic-Opara N, Malak S. Tensile behavior of slurry infiltrated mat concrete (SIMCON). ACI Mater J 1997;94(1):39–46.
[11] Bayasi Z, Zeng J. Flexural behavior of slurry infiltrated mat concrete (SIMCON). J Mater Civil Eng 1997;9(4):194–9.
[12] Rossi P. High performance multimodal fiber reinforced cement composites (HPMFRCC): the LCPC experience. ACI Mater J 1997;94(6):478–83.
[13] Li VC. From micromechanics to structural engineering – the design of cementitious composites for civil engineering applications. Struct Eng Earthquake Eng 1994;10(2):1–34.
[14] Maalej M, Li VC. Flexural/tensile-strength ratio in engineered cementitious composites. J Mater Civil Eng 1994;6(4):513–28.
[15] Maalej M. Fracture resistance of engineered fiber cementitious composites and implications to structural behavior. PhD thesis 2004, University of Michigan, at Ann Arbor, Michigan, USA.
[16] Naaman AE, Shah SP. Tensile tests of ferrocement. J Amer Concrete Inst 1971;68(9):693–8.
[17] Peled A, Mobasher B. Pultruded fabric–cement composites. ACI Mater J 2005;102(1):15–23.
[18] Mobasher B, Peled A, Pahilajani J. Distributed cracking and stiffness degradation in fabric–cement composites. Mater Struct 2006;39(287):317–31.
[19] Mobasher B, Pahilajani J, Peled A. Analytical simulation of tensile response of fabric reinforced cement based composites. J Cement Concrete Compos 2006;28(1):77–89.
[20] Aldea CM, Mobasher B, Jain N. Cement-based matrix-grid system for masonry rehabilitation. SP-244-9, ACI Special Publications; 2007. p. 141–55.
[21] Majumdar AJ, Laws V. Composite materials based on cement matrices. Phil Trans R Soc Lond A 1983;310:191–202.
[22] Soranakom C, Mobasher B. Closed-form moment–curvature expressions for homogenized fiber-reinforced concrete. ACI Mater J 2007;104(4):351–9.
[23] Soranakom C, Mobasher B, Bansal S. Effect of material non-linearity on the flexural response of fiber reinforced concrete. In: Proceeding of

the eighth international symposium on brittle matrix composites BMC8, Warsaw, Poland; 2006. p. 85–98.
[24] Soranakom C, Mobasher B. Closed form solutions for flexural response of fiber reinforced concrete beams. J Eng Mech 2007;133(8):933–41.
[25] Ulfkjaer J, Krenk S, Brincker R. Analytical model for fictitious crack propagation in concrete beams. J Eng Mech 1995;121(1):7–15.
[26] Olesen JF. Fictitious crack propagation in fiber-reinforced concrete beams. J Eng Mech 2001;127(3):272–80.
[27] Swamy RN, Al-Ta'an SA. Deformation and ultimate strength in flexural of reinforced concrete beams made with steel fiber concrete. ACI Struct J 1981;78(5):395–405.
[28] Hassoun MN, Sahebjam K. Plastic hinge in two-span reinforced concrete beams containing steel fibers. Proc Can Soc Civil Eng 1985:119–39.
[29] Noguchi K, Matsuda Y, Oishi M. Strength analysis of Yttria-stabilized tetragonal Zirconia polycrystals. J Am Ceram Soc 1990;73(9):2667–76.